A portable 3D Imaging FMCW MIMO Radar Demonstrator with a 24x24 Antenna Array for Medium Range Applications

Alexander Ganis*‡, Enric Miralles*, Bernhard Schoenlinner*, Ulrich Prechtel*, Askold Meusling‖, Christoph Heller*, Thomas Spreng*, Jan Mietzner†, Christian Krimmer†, Babette Haeberle†, Martin Maier†, Steffen Lutz†, Christian Weckerle†, Heinz-Peter Feldle†, Mirko Loghi‡, Angel Belenguer¶, Hector Esteban§ and Volker Ziegler*
*Airbus Group Innovations
Willy-Messerschmitt-Str. 1, Taufkirchen, Germany 82024
Email: alexanderrudolf.ganis@airbus.com, enric.miralles-navarro@airbus.com
‖Airbus Defence and Space, Woerthstrasse 85, Ulm, Germany 89077
†Airbus Defence and Space Electronics and Border Security, Woerthstrasse 85, Ulm, Germany 89077
‡University of Udine, Via delle Scienze 206, Udine, Italy 33100
§Universidad Politecnica de Valencia, Camino de Vera, s/n, Valencia, Spain 46022
¶Escuela Politecnica de Cuenca, Campus Universitario, s/n, Cuenca, Spain 16071

***Abstract*—Multiple-Input-Multiple-Output (MIMO) radars have been shown to improve target detection for surveillance applications thanks to their proven high performance properties. In this paper, the design, implementation and results of a complete three-dimensional (3D) imaging Frequency Modulated Continuous Wave (FMCW) MIMO Radar demonstrator are presented. The radar sensor working frequency range spans between 16 GHz and 17 GHz and the proposed solution is based on a 24 transmitters and 24 receivers MIMO radar architecture, implemented by time division multiplexing (TDM) of the transmit signals. A modular approach based on conventional low cost Printed Circuit Boards (PCB) is used for the transmit and receive system. Using digital beam-forming (DBF) algorithms and radar processing techniques on the received signals, a high resolution 3D sensing of the range, azimuth and elevation can be calculated. With the current antenna configuration, an angular resolution of 2.9° can be reached. Furthermore, by taking advantage of the 1 GHz bandwidth of the system, a range resolution of 0.5 m is achieved. The radio-frequency (RF) front-end, digital system and radar signal processing units are here presented. The medium range surveillance potential and the high resolution capabilities of the MIMO radar are proven with results in the form of radar images captured from on the field measurements.**

***Index Terms*—Multiple-input-multiple-output (MIMO), Radar, Frequency Modulated Continuous Wave (FMCW), Time Domain Multiplexing (TDM), three-dimensional (3D), Digital Beam-Forming (DBF), Printed Circuit Boards (PCB).**

I. Introduction

Imaging radar systems are crucial solutions for detection, tracking and classification of targets in airborne, surveillance and ground based applications. This is mainly due to their high performance under various weather conditions, material penetration properties and usability at day and night, compared to other sensors, such as lasers and cameras based systems. Different imaging radar solutions exist. Mechanically steered radars are usually complex systems because of their physically moving components and long term reliability is often compromised. Synthetic aperture radars (SAR) are a good solution that uses the motion of the radar antenna over a targeted region [1]. This leads to a finer cross-range resolution, but there is a need for a continuously moving platform. Radars need a large effective aperture of the antennas in order to achieve a high resolution. This can be achieved in classical phased array radars [2], with a high number of elements along the transmit and receive paths, which tends to be a relatively large, complex and expensive approach.

Better performance can be achieved by utilizing a MIMO architecture [3],[4]. In a MIMO system, orthogonal signals are emitted from the transmit antennas and jointly processed at the receivers. The signal orthogonality can, for example, be established in time-domain by employing a TDM scheme switching between the transmit antenna elements. The typical scheme, usually a round-robin structure, consists in activating only one transmit antenna element at a time, starting from the first one and then progressively sweeping through all. Upon reaching the last antenna element, the scheme is repeated from the beginning. In particular, this allows the calculation of amplitude and phase relationships of a large number of points in space, which is the result of multiplication of the number of transmit by the number of receive elements. These points form the elements of the virtual antenna array.

The MIMO principle together with an appropriate antenna array arrangement enables an improvement in the cross-resolution by an artificial increase of the antenna aperture with the so called virtual array concept. Therefore, in combination with a signal with a large bandwidth, which determines the resulting resolution in the range direction, high-resolution

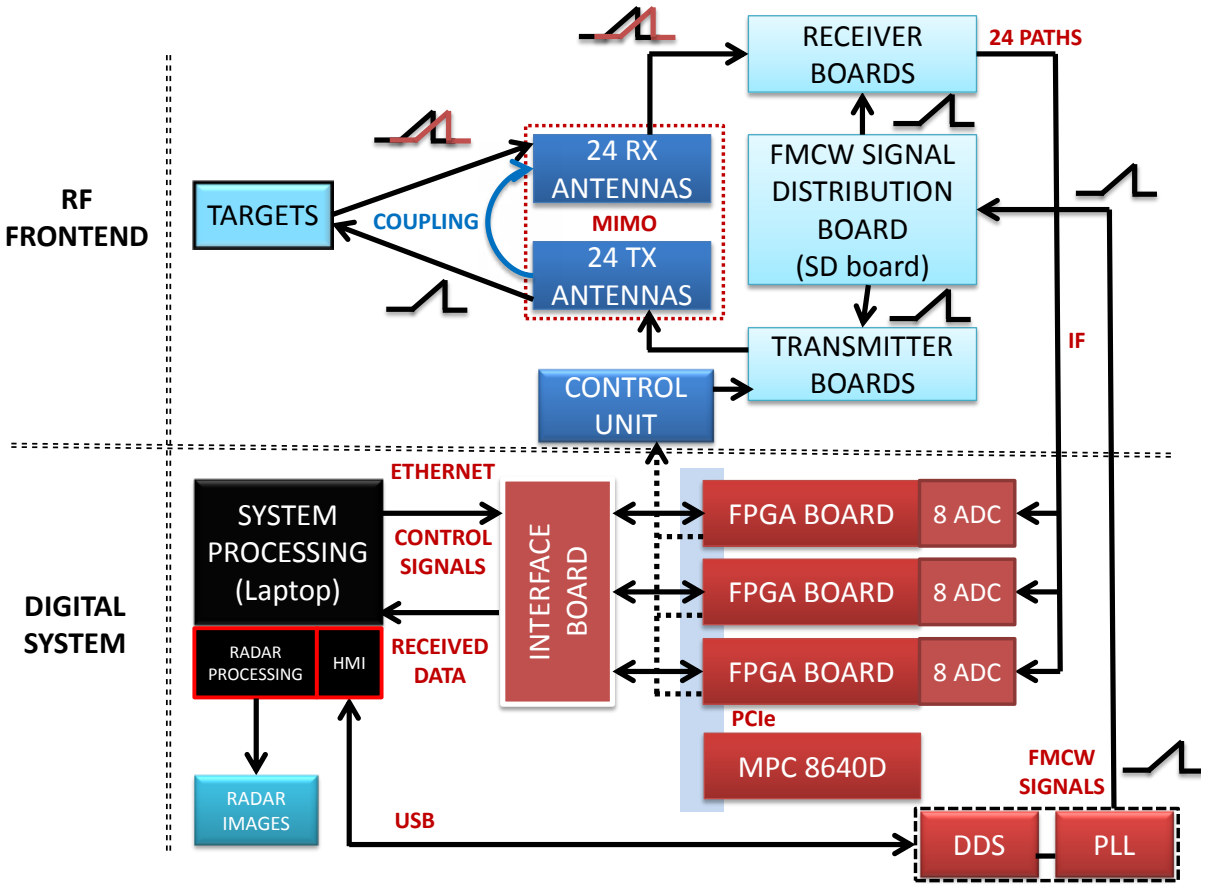

Fig. 1. Block diagram of the 3D Imaging FMCW 24x24 MIMO Radar Demonstrator.

3D images of the captured scenario can be achieved in a smaller sized radar. The applications that our 3D imaging MIMO radar demonstrator is intended for, are the ground based surveillance of stationary wide-zones and high security or hazardous infrastructures like chemical and nuclear plants, fuel transmission and energy pipelines and, more in general, applications in remote areas where a portable platform is highly desired.

Several MIMO radars have been proposed [5]-[17], nevertheless literature shows that a 1 GHz broadband system as the one proposed here, has been achieved only by few, namely in [5], [13], [14] and [15] with a bandwidth of 8 GHz, 1 GHz, 1 GHz and 1 GHz, respectively. A 2D MIMO array granting the ability to reconstruct 3D images with both azimuth and elevation information has been accomplished in a full imaging demonstrator only in [5] and [16]. However, these solutions are only suitable for short range applications, i.e. for distances up to 20 meters or less, which are not targeted in this work.

In this paper, a complete 3D MIMO imaging radar demonstrator which operates with a 24x24 MIMO 2D antenna array configuration is presented. A complete system integration of the RF frontend, the digital system and the software architecture for digital signal processing has been accomplished. Additionally, the demonstrator has been designed to be compact and portable by including its own power unit and cooling system. Moreover, the radar system is intended to be flexible as much in its hardware as it is in its software. A modular approach based on conventional low cost PCB is used for the transmit and receive boards. This modular approach is based on RF multilayer panels with integrated antennas, that are easily stackable in a sandwich configuration. This grants the possibility to vary the number of antennas by removing or adding panels, thus varying the angular resolution and the size of the radar, until the desired values are reached. From the software side, the FMCW radar signal parameters can easily be adapted in order to create complete 3D images or only cuts of the complete data for faster radar processing times. The measured radar sensor working frequency range spans between 15 GHz and 17.5 GHz with FMCW signals having an operational bandwidth of 1 GHz [10],[11]. The system is flexible, compact and portable, thus a new range of applications can be explored.

The system architecture of the radar system is presented in the following sections together with an in depth description, measurements and pictures of the RF front-end components. Furthermore, a detailed description of the implemented digital system, the radar signal processing and the image reconstruction techniques is provided. Finally, radar measurements and

images taken from a real test scenario are shown together with a comprehensive evaluation of the radar's performance and its target detection capabilities.

II. System Architecture

The top-level system structure of the built MIMO radar demonstrator is presented in the form of a block diagram in Fig. 1. Here, the two main building blocks can be seen: the RF frontend and the digital system. In a FMCW radar, operating with a TDM architecture, a sine carrier is swept across the radar bandwidth and sequentially sent through the different transmit antennas. After receiving the chirp signals from the receive antennas, the receivers down-convert the received signal by means of mixing with the transmit chirp signal, so that the signal runtime differences from different reflectors in the scenery translate into different so called beat frequencies. These signals are then sampled and processed in order to generate 3D radar images of the captured scenario. The chirps used in this MIMO radar demonstrator are signals which frequency increases (up-chirps) with time from 16 GHz to 17 GHz, in 100 µs.

The RF front-end system is the essence of the transmit and receive signals analog operations. It consists of the transmit boards, the receive boards, the transmit and receive antenna arrays and the FMCW Signal Distribution (SD) board. The FMCW SD board provides the chirp signals that are used for transmission and the reference signals for the de-ramp mixing technique used in our radar, where the mixing occurs between the received chirp signals at the RX array and the transmitted chirp replica coming from the FMCW SD board. The comprehensive description of the RF frontend is given in Section III.

The signal processing is at the core of the digital system, which consists of a system processing program on a laptop for radar control and radar signal processing, a combined Direct Digital Synthesizer (DDS) and Phase-Locked Loop (PLL) system for the generation of the configurable transmit waveforms and three Field Programmable Gate Array (FPGA) cards with ADC units for parallel hardware-based signal acquisition, radar signal processing and radar image generation. A complete description of the digital system will be given in Section IV. A graphic Human-Machine Interface (HMI) on the system processing workstation sends the signal generation parameters to the DDS and PLL element and the generated FMCW signals are distributed by the FMCW SD board to the transmitter boards and antennas. The control unit selects individual transmit antenna elements in order to apply TDM. The signals reflected from the targets are received through the receiver antennas with multiple receive paths and are processed in parallel in the digital unit. The pre-processed data is then sent back to the offline software based radar signal processing functions on the workstation that apply digital beam-forming techniques to generate the final radar images.

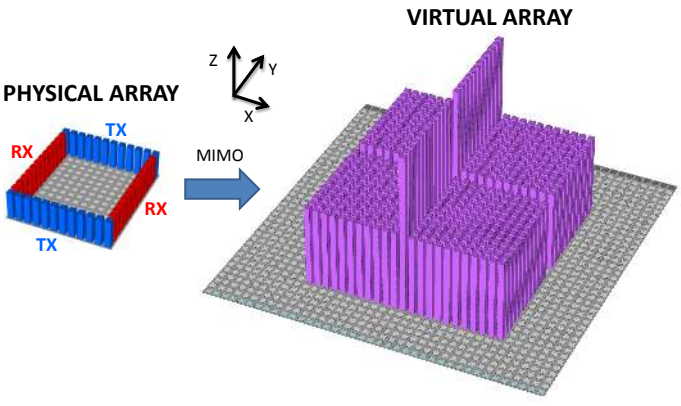

Fig. 2. Schematic representation of the MIMO antenna configuration with the physical array (left) showing the 24 TX antennas in blue, the 24 RX antennas in red and the resulting virtual array (right).

III. The RF Frontend

The focus of this section is on the RF front-end. The hardware was optimized for a frequency range of 16 GHz to 17 GHz, which is allocated in Germany for non-navigational radio-location services.

A. MIMO Array Configuration

The presented MIMO radar consist of two sets of multiple transmit (TX) and receive (RX) antennas. Orthogonality between the transmitted signals of the channels is obtained through the use of a TDM architecture of the transmitters. The equivalent virtual array can be calculated as the discrete convolution of the overall RX and TX element positions.

In this work, the fabricated antenna elements are based on Tapered Slot Antennas (TSA) [18]. Fig. 2 depicts the positions of the antennas' phase centers and the corresponding MIMO virtual array. RX elements (in red) and TX elements (in blue) are placed forming a rectangle. In this manner, the equivalent virtual array has four times the surface of a fully populated array with the same perimeter. This leads to an improvement in the resolution of a factor of two in each axis. Thus, the angular resolution is approximately expressed as [19]

$$\Delta\theta_{3dB} \approx 50^\circ \frac{\lambda_0}{d2N} \approx 2.5^\circ \quad (1)$$

with λ_0 being the wavelength, N the number of elements of an equivalent fully populated array with the same perimeter as our physical array and d the distance between elements. The higher purple bars in the right of Fig. 2 are redundancy elements. Concerning the redundant elements, there are two important aspects that need to be considered. First, the redundant elements are simply discarded in the beam-forming and image generation algorithms of the processing unit, therefore not harming the reconstructed radar image. Second, in some fast-moving scenarios the switching time could be slower than the image changes. As a consequence of the redundancy, the same virtual element is calculated at two different times. This can be exploited in order to evaluate if the radar images are fitting the reality. Defining corresponding algorithms will be one important aspect of our future work. Regarding the empty row which appears in the center of Fig. 2, an interpolation of

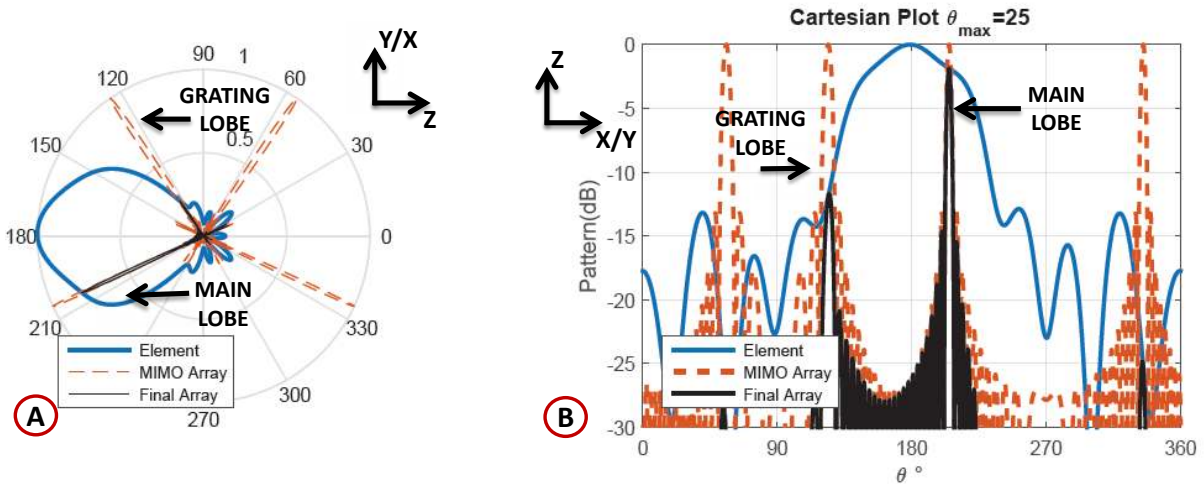

Fig. 3. The graph illustrates a simulation of virtual array pattern with the designed maximum beamsteering of $\theta_0 = 25°$ in red, the single element in blue and the resultant multiplication of both in black. The patterns are displayed in polar (subfigure A) and cartesian (subfigure B) coordinates.

the data is performed, according to what has been previously described in [21].

In order to reduce the coupling between radiating elements and to increase the angular resolution, the distance between antennas was chosen greater than $\frac{\lambda_0}{2} = 9.7$ mm. Consequently, grating lobes appear. Since the desired Field Of View (FOV) is $\pm 25°$, the system was optimized placing the elements with $d_y = d_x = 15$ mm of spacing. In such a manner, the grating lobes are outside the desired field of view and, based on simulations, an improvement of approximately 10 dB in the coupling is achieved, compared to a spacing of 9.7 mm.

Fig. 3 presents a calculation of the resultant antenna pattern. Subfigure A is dedicated to the antenna pattern of the virtual array in polar coordinates (dashed curve) with the maximum beam steering of $\theta_0 = 25°$, single element in blue and the resultant multiplication. As the image shows, the grating lobe remains under -12 dB on the desired FOV. In subfigure B, the same curve is plotted in cartesian coordinates. Since the beam-forming is carried out at the digital signal processing side with a delay-and-sum beamformer algorithm, no phase shifters are needed.

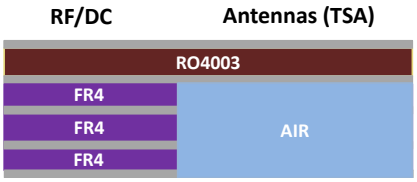

Fig. 4. Representation of the used layer stack-up.

B. Transmitter

The layer stack-up of the boards used in this paper is presented in Fig. 4. The RO4003 material is a high frequency suitable material from Rogers corporation with $h = 0.203$ mm, $\epsilon_r = 3.55$ and $\tan\delta = 0.0027$. The main function of the Flame Retardant (FR4) ($h = 1$ mm) is to give physical stability. The FR4 also allows to add extra metal layers for routing of Direct Current (DC) signals.

A switch chain with a built-in gain of $G_{TX} = 19$ dB is responsible for the selection of the dedicated antenna at the proper time, according to the employed TDM scheme. The switches are Commercial Off The Shelf Components (COTS) with 1.6 dB insertion loss and 41 dB isolation, at 16.5 GHz [22]. The switching process is controlled by the firmware's procedures of the digital system by means of setting a Complex Programmable Logic Device (CPLD).

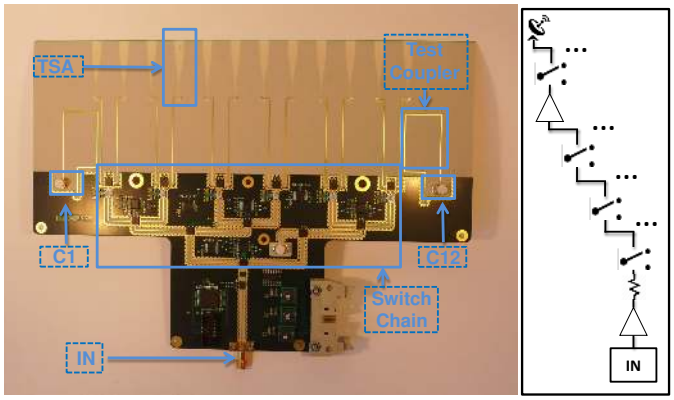

Fig. 5. Photograph of the complete TX panel (left) and the corresponding block diagram (right).

Fig. 5 illustrates the transmitter board and its circuit diagram. The switch chain is located in between the input connector and the antennas. A single path of the switch chain, shown on the right side of Fig. 5, which contains two amplifiers, an attenuator, four switches, an antenna and a 20 dB test coupler (only the first and last paths).

Test measurements of the board are performed with a network analyzer, which has 2 ports with its corresponding cables terminated with a K coaxial connector. A through-

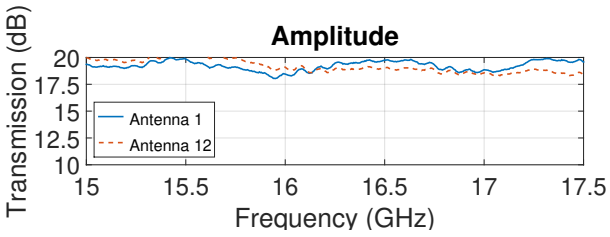

Fig. 6. S-Parameters of the transmission from antenna 1 and 12. The effects of the coupler are compensated.

reflect-line calibration (TRL) is performed at the level of its cables. Fig. 6 shows S-Parameters from port IN to C1 and C12, which are the ports of the test coupler shown in Fig. 5. A K coaxial to Mini-coaxial transition is included in the measurements but it has a minor impact. A correction factor of 20 dB, due to the test coupler, is also applied. The gain of the board well fits the designed value of $G_{TX} = 19$ dB. A difference in amplitude smaller than 1.25 dB can be observed.

C. FMCW Signal Distribution (SD) Board

The FMCW SD board, illustrated in Fig. 7, provides a phase-coherent signal from a single input port to 16 output ports (14 for the RX and TX boards and 2 for testing purposes). The output ports are directly connected to the FMCW input ports of each RX and TX board. The FMCW SD board is fabricated with 4 stages of single resistor Wilkinson power splitters and two stages of commercial amplifiers. Fig. 7 shows a picture of the fabricated PCB and its corresponding schematic, on the upper part of the image.

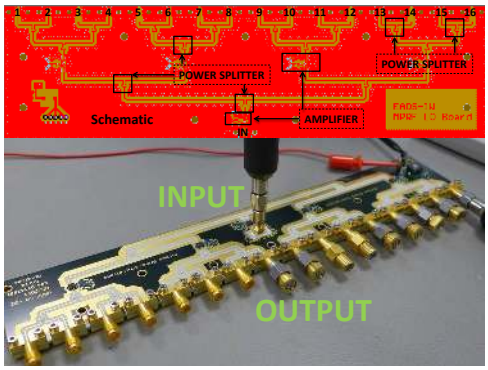

Fig. 7. Photograph of the FMCW signal distribution board with its 16 output ports.

The substrate described in Fig. 4 is also used for this board.

The FMCW SD board is measured with a network analyzer. A TRL calibration is performed at the level of its cables. As it can be observed in Fig. 7, a transition from K to mini coaxial connector is needed at the input port. The effects of this transition are minor and are included in the measurements.

The transmission amplitude and phase of all 16 channels belonging to the FMCW SD board are depicted in Fig. 8 and Fig. 9, respectively. As shown in Fig. 8, a maximum difference of 0.5 dB in the amplitude is measured. Moreover,

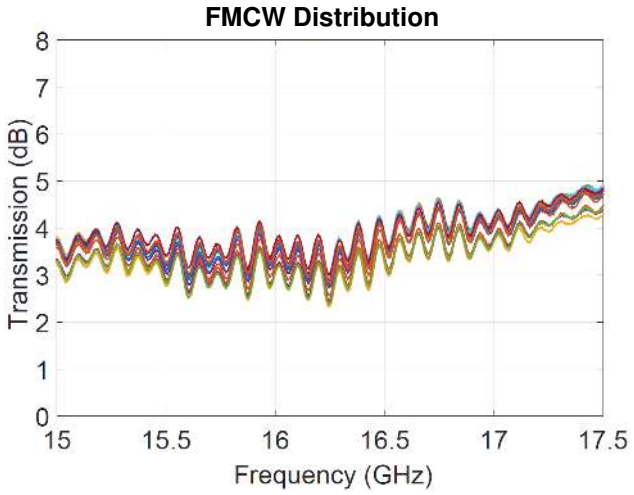

Fig. 8. Amplitude comparison between all channels of the FMCW distribution board.

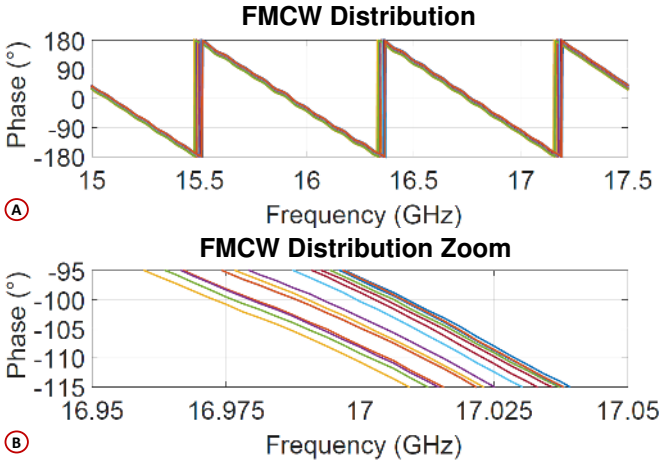

Fig. 9. Phase comparison between all channels of the FMCW distribution board.

it can be seen from Fig. 9, subsection B, that a maximum difference of 13.3° in the phase is also measured. These differences are due to tolerance errors in the PCB fabrication process, its components tolerances and because of soldering inhomogeneities. Nevertheless, these differences do not affect the performance of the system since a digital processing post calibration is applied in order to overcome the small disparities.

D. Receiver

The substrate described in Fig. 4 is also used for the receiver. A picture of one of the fabricated boards is shown in Fig. 10, in which the key components such as the TSA elements, mixer, low-noise amplifier (LNA), FMCW signal path, anti-aliasing filter and equalizer are highlighted. As known from the classic FMCW theory [11], a sine carrier is swept across the radar bandwidth and the receiver down-

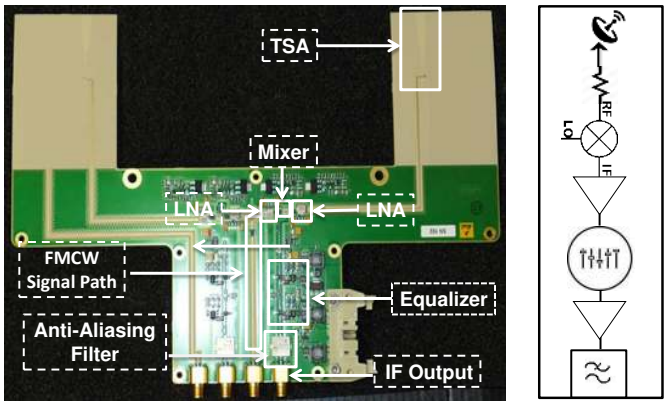

Fig. 10. Photograph of the receiver board, on the left, and corresponding block diagram, on the right.

converts the received signal by means of mixing with the transmit signal, coming from the FMCW signal path, so that the signal runtime differences from different reflectors in the observed radar scenery translate into different intermediate frequencies (IF).

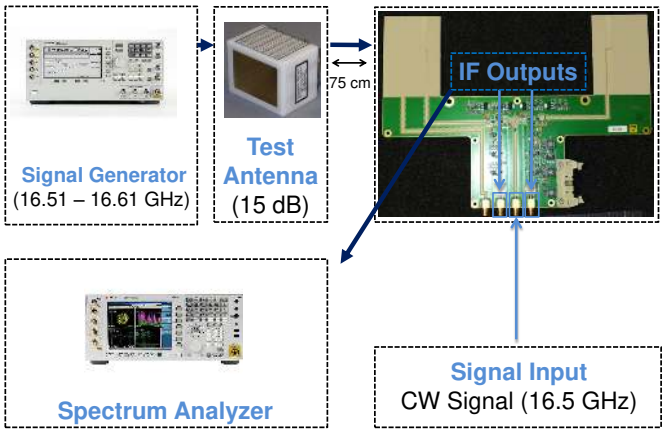

Fig. 11. Measurement setup for testing the performance of the receiver board and the equalizer.

Over the whole frequency band of operation, the attenuation of the received signal is different, considering that the down-converted signals produced by more distant targets show lower amplitude and higher beat frequency. In order to compensate this, a passive equalizer is incorporated in the receiver design. A measurement setup is created in order to analyze the IF output performance of the RX board, as illustrated in Fig. 11. A signal generated from a vector signal generator with a frequency range from 16.51 GHz to 16.61 GHz is fed to a test horn antenna with 15 dB gain, which is placed at a range of 75 cm from the antennas on the RX board. The FMCW input on the RX board is excited with a continuous-wave (CW) signal at 16.5 GHz and the IF output ports are then connected to a spectrum analyzer. The results are shown in Fig. 12, which represents a screenshot taken directly from the

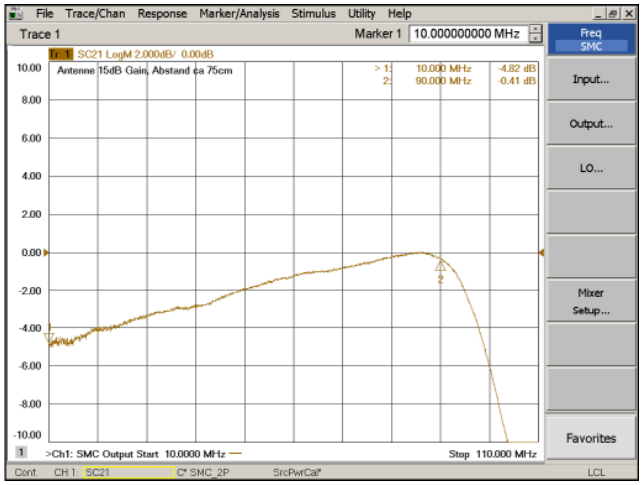

Fig. 12. Screenshot of the measurement of the IF output performance of the RX board, captured by a spectrum analyzer.

spectrum analyzer. In this picture, the effects of the equalizer are clearly visible, as an attenuation on the amplitudes of the signal that starts stronger in the lower frequency range and whose effect is linearly decreasing, in order to compensate the higher losses in amplitude for higher frequencies. The low pass filtering effect (beyond 100 MHz at marker number 2 of Fig. 12) is instead caused by the anti-aliasing filter.

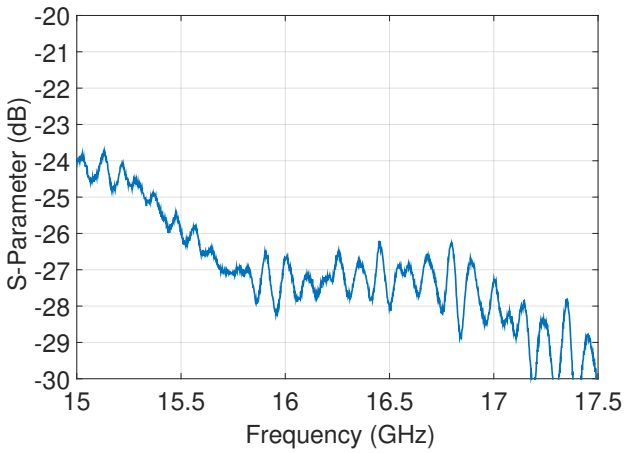

Fig. 13. Measured maximum coupling between one TX and one RX antenna. The chosen elements were adjacent, with a distance (d) of 15 mm.

E. Coupling Between Antennas

The mutual coupling between antenna elements, in particular between TX and RX elements, is a well known and undesired effect of radar systems, especially for FMCW. When a signal is transmitted from a TX antenna, a part of the signal couples with an adjacent RX antenna and this may compromise the performance of the overall radar system. The maximum coupling between the antennas, with the chosen configuration for our system, is smaller than $C < -23$ dB in the frequency range of operation, as illustrated in Fig. 13.

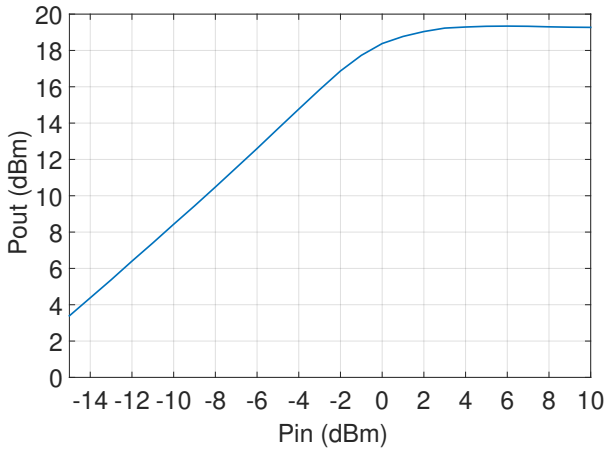

Fig. 14. Measured input power versus output power in the transmitter board. The measurement was performed from the input to the coupler C1 before the antenna. The effects of the coupler are compensated.

This undesired coupled power can saturate the mixer. In order to avoid this malfunction, the RF power at the mixer must be below $P_{1dB_{MIX}} = 11$ dBm. Considering that the gain of the LNA is $G_{LNA} = 19$ dB and the losses in the line between the receiver antenna and the LNA are $L = 2.5$ dB, the maximum sustainable power at the receiver antenna would be $P_{RX_{MAX}} = -5.5$ dBm. Using the following equation

$$P_{TX_{OUT}} = P_{RX_{MAX}} + C \tag{2}$$

a maximum transmit power of $P_{TX_{OUT}} = 20.5$ dBm results. Fig. 14 shows the measured input power versus output power with compensated effects of the test coupler in the transmitter board. As a conclusion, the coupling does neither damage nor affect the performance of our system because even if a strong signal is sent to the input of the receiver, the amplifiers at the transmit board saturate and will always provide a signal with a power below $P_{TX_{OUT}} < 20.5$ dBm.

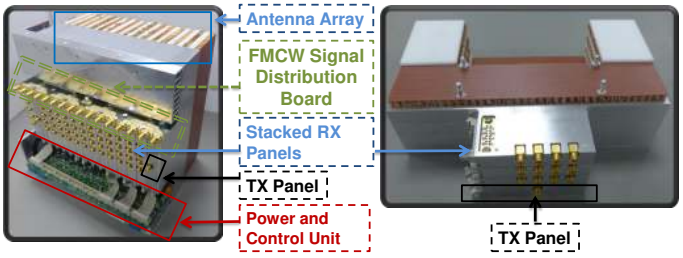

Fig. 15. Photographs of the stacked TX, RX and FMCW signal distribution panels. The left image shows the complete RF front-end unit. The right image is a section view of its structure.

F. Assembly of the RF system

The RX, TX and FMCW signal distribution modules are built on panels, as shown in Fig. 15, which are stacked horizontally, in such a way that the desired antenna configuration is achieved. Each RX and TX panel structure is the result of the composition of a multilayer PCB, stacked with a 7 mm thick honeycomb board, a 4 mm Rohacell foam stabilization system and a metal support.

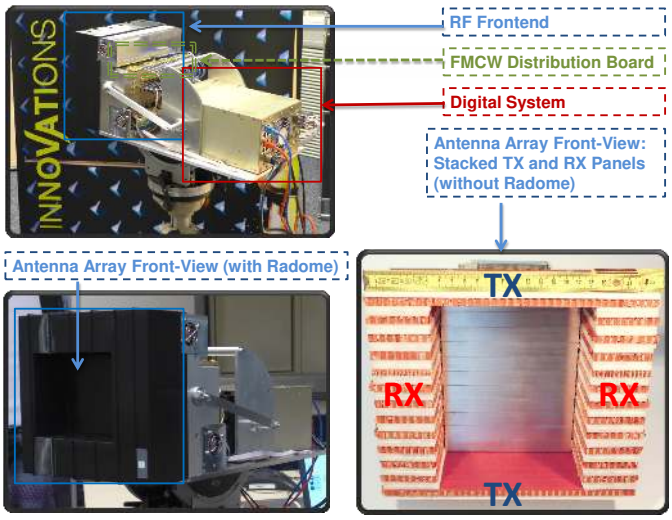

Fig. 16. Photographs of the complete MIMO radar system. In the upper left image, the integrated RF front-end and digital system is presented. On the lower left and right images, a front view of the antenna array is shown.

In the upper left part of Fig. 16, the complete configuration of the 24x24 MIMO radar demonstrator is illustrated. In this part of the image, it is possible to see the assembled RF front-end and the digital system unit. The lower part of the figure shows the antenna array front view with the radome protection, on the left, and without the radome protection, on the right. In this lower right part of the image, the stacked RX and TX panels configuration can be seen from a front view.
In order to achieve a compact and portable radar, a power unit and cooling system have been integrated into the system, as it can be seen from Fig. 15. The system operates with 24 V and a maximum current use of 5.6 A, therefore yielding a maximum power consumption of 134 W.

IV. Digital System

An overview of operation of the digital processing system is presented in the form of a block diagram in Fig. 1. Here, the main units of the digital system are illustrated: the FPGA boards, the ADC units, the PowerPC, the DDS and PLL unit and the offline system processing block. The purpose of the following paragraphs is to describe the digital system hardware and software architecture, its functionalities and the offline radar signal processing software on the laptop workstation for the 3D image reconstruction of the radar captures.

A. Hardware Architecture

As illustrated in Fig. 1, for the hardware realization of the digital signal processing part, three Virtex-5-SX95T [23] FPGA based cards are used. The cards are joined with FPGA Mezzanine Cards (FMC) FMC108 boards by 4DSP [24]. Each

of the cards is equipped with an 8 channel ADS62P49 ADC that provides eight analog to digital 14 bit 250 Mega-Samples-Per-Second (MSPS) channels. The sampling clock for the ADCs is supplied externally, directly from the DDS and PLL board. A picture of the digital system is shown in Fig. 17. The available trigger input for customized sampling control is used. This is of high importance since the 24 channels from the 3 boards combined must be perfectly synchronized in order to achieve coherence and perform beam-forming on the received signals. The custom built operational firmware sets all 24 ADC cards to operate with a sampling clock of 204.8 MHz. Additionally, a Freescale MPC8640D [25] dual-core processor for overall data management and transfer is adopted.

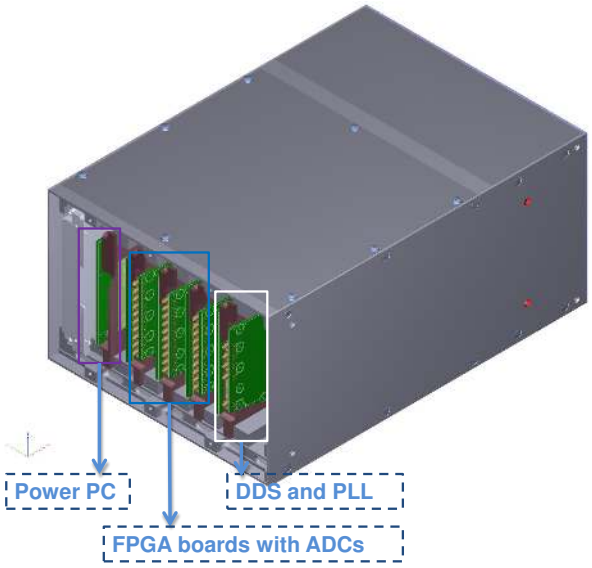

Fig. 17. 3D illustration of the complete digital unit with the 3 FMC-FPGA boards, the PowerPC and the DDS and PLL board.

B. Software Architecture

A custom built VHSIC-Hardware-Description-Language (VHDL) coded firmware has been implemented that works seamlessly with the embedded software on the PowerPC through a Peripheral Component Interconnect Express (PCIe) interface. Additionally, the signal generation through the DDS and PLL blocks are controlled from the MIMO radar control graphic HMI through a Universal Serial Bus (USB) interface. The data sent from the HMI to the DDS consist of control parameters for the characteristics of the transmitted FMCW radar signals, such as the start and stop frequencies and the duration of the signal. Throughout the measurements, start and stop frequencies of 16 GHz and 17 GHz, respectively, and a signal duration of $100\,\mu s$ have been used. Therefore, the resulting waveform is an up-chirp signal, generated by a sine carrier which is continuously swept across a 1 GHz radar bandwidth in $100\,\mu s$.

Moreover, the HMI exchanges data with the FPGAs directly. The data consist of various register control settings, radar control parameters, number of measurements to be taken and antenna settings. Taking into consideration the concept of TDM used throughout our radar system [26], there is a need to switch between each transmit antenna within a very small time slot while all other transmit antennas are switched off in order to keep the frequency modulated signals mutually orthogonal so that no interference occurs. Therefore, after initial load of parameters to the DDS and the FPGA, the signal generation is started and the first of the transmit antenna is selected. The up-chirp signal is continuously running and each up-chirp starts matched with a trigger signal.

The next step is the sampling of each received radar signal. The radar echo signal is processed in each receive chain simultaneously. Due to the the TDM architecture used, only one transmit antenna element is active at each time. Therefore each receiver can separate all signals transmitted by the different antennas. The sampling is performed by the 8 ADCs of one board on the received signals and generates sampled signals of 32768 samples that are stored inside Random-Access Memory (RAM) blocks, internally to the FPGA. The FPGAs custom firmware is built in such a way that the sampling is initiated on the rising edge of an up-chirp signal and therefore, is synchronized across the 8 ADCs. Moreover, synchronization is preserved also across FPGAs through a master-slave configuration where an FPGA is selected to be the master and receives the external reference clock provided by the DDS and PLL unit and routes it, together with the trigger signal, to the other FPGAs. The firmware process ends after activating all transmit antennas and capturing the radar signals on all receive paths.

The received samples are then fed through the PCIe interface to a MPC8640D unit that processes the data from the FPGAs and creates a binary file which contains the raw data matrix i.e., the combination of 24 transmit signals by 24 receivers by 32768 samples of 14 bit each. The raw data matrix file is then transferred automatically via Ethernet to the radar processing system realized under MATLAB™.

C. Radar Digital Signal Processing

A total of 576 signals are read from the binary file into MATLAB™, into a 3D matrix of 24 x 24 x 32768 elements, corresponding to the number of transmit antennas, the number of receive antennas and the total number of samples per signals, respectively. For each subset of transmit and receive elements (T_n, R_n), the 32768 samples represent the transmitted chirp signals from transmit antenna T_n and received at receive antenna R_n. However, of all the 32768 samples acquired, only 20480 samples are of interest. The number of samples for one chirp is given by the chirp duration in time, $t_{chirp} = 100\,\mu s$, multiplied by the sampling frequency, $f_s = 204.8$ MHz. Thus, in a first step, a filtering operation is conducted in order to extract only the information of one chirp signal. The result is a matrix which is now reduced to 24 x 24 x 20480 samples. Subsequently, the 576 signals are windowed through the use of a Hanning window in order to reduce the side lobes in both range and azimuth direction

[20], Hilbert transformed and down converted to baseband. The outcome is a 3D matrix of 576 windowed and complex-valued signals.

D. Calibration

Considering that certain elements of the matrix show different time delays, due to intolerances and different path lengths of the cables in the system, a calibration was performed in order to reduce the influence of systematic measurement errors on the image reconstruction. Therefore, the first step of the calibration consists in the correction of these constant phase offsets. The corrections are applied to a subset of complex signals of the matrix by means of a multiplication for a complex exponential containing the time correction.

The second step is the creation of a calibration matrix. In order to generate this, a real data measurement of a simple test scenario with one corner reflector at 37 m and at $0°$ of both azimuth and elevation, is multiplied for the conjugate of the same scenario, simulated idealistically in the MATLAB environment. The resulting calibration matrix is then used, by means of multiplication, with all new radar measurements in order to correct the systematic measurement errors from hardware.

Regarding the sensitivity of the radar to external factors throughout different radar captures, as long as the receiver channels change approximately equally through time, i.e. they are almost equally affected by temperature changes, no recalibration is necessary, considering also that our performed tests have shown that the calibration measure taken is still valid after months of radar operation.

The result is a calibrated 3D matrix where each signal phase is perfectly linear and represents the input for the digital beam-forming algorithm [3]. The complete MIMO matrix can be seen as

$$M_{IF} = [M_{IF}[1], M_{IF}[2], ..., M_{IF}[N_{virtual}]] \tag{3}$$

which is a $N \cdot N_{virtual}$ matrix whose columns $M_{IF}[i]$ with $(i = 1, ..., N_{virtual})$ are the complex time domain chirp signals with N sampled points of each virtual element and $N_{virtual} = N_{TX} \cdot N_{RX}$ represents the size of the virtual array, a multiplication of the number of transmit elements by the number of receive elements. The Cartesian position of the virtual elements is obtained by convolution of the real TX and RX antenna elements, as previously shown in Fig. 2.

E. Image Reconstruction

The image processing technique chosen for the proposed radar system is a combination of two core functions. The first one is a Fast Fourier Transform (FFT) in frequency direction in order to determine the range profile of the object, which is contained in the channel impulse response. The second one is a delay-and-sum beam-former function system for azimuth and elevation processing which is used to reconstruct the scene imaged by the MIMO radar sensor [21],[27]. The image processing function operates on the 3D calibrated matrix given in (3) and starts with calculating the range compressed data

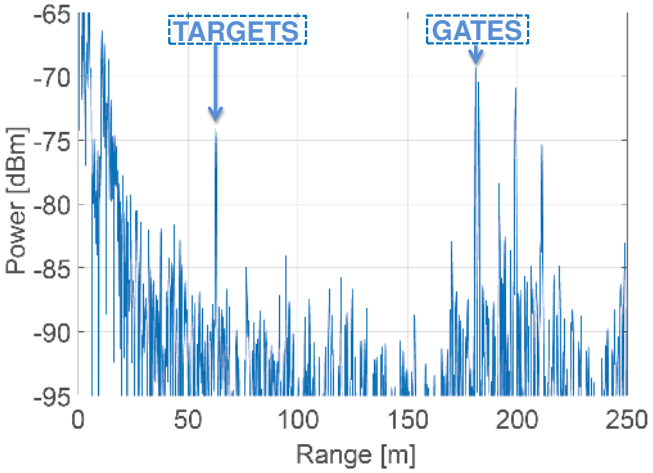

Fig. 18. Range compression through FFT of the received signal from one of the virtual elements.

matrix $\widetilde{M}_{IF}$ by means of an FFT transform in time direction. As an example, the result of the FFT operation on one of the received signals of the virtual array is presented in Fig. 18, where a distinguishable peak can be seen at 60 m. The position of the peak is the same for the two targets, which are the two corner reflectors at the same distance, in the radar test field used and shown in Fig. 20. Other peaks are visible in this image, which represent surrounding objects, such as metal gates which were present in the background of the scene of radar capturing.

The following step is the application of a delay and sum beam-forming algorithm that compensates the phase shift of each virtual element belonging to the virtual array, according to a weighting vector

$$\begin{aligned} w(\theta,\phi) = [&e^{j2\pi\frac{f_0}{c_0}x_v(1)\sin(\theta)\cos(\phi)+y_v(1)\sin(\theta)\sin(\phi)}, \\ &e^{j2\pi\frac{f_0}{c_0}x_v(2)\sin(\theta)\cos(\phi)+y_v(2)\sin(\theta)\sin(\phi)}, ..., \\ &e^{j2\pi\frac{f_0}{c_0}x_v(N_{virtual})\sin(\theta)\cos(\phi)+y_v(N_{virtual})\sin(\theta)\sin(\phi)}] \end{aligned} \tag{4}$$

where x_v and y_v are the positions of the virtual elements in the x and y axis, respectively, and θ and ϕ denote the angle of arrival of a given point target in azimuth and elevation, respectively. Therefore, the beam-forming operation can be seen in a vector notation as

$$\hat{m}(\theta,\phi) = \widetilde{M}_{IF} w(\theta,\phi) \tag{5}$$

which represents the image of the signal received from angles θ (azimuth) and ϕ (elevation), giving a full 3D representation of the scenario. The angles are expressed with respect to the bore-sight of the radar, for which $\theta = 0°$ and $\phi = 0°$.

F. Timings Considerations

The TDM technique used in this radar demonstrator, consisting in the switching between the transmit antenna elements

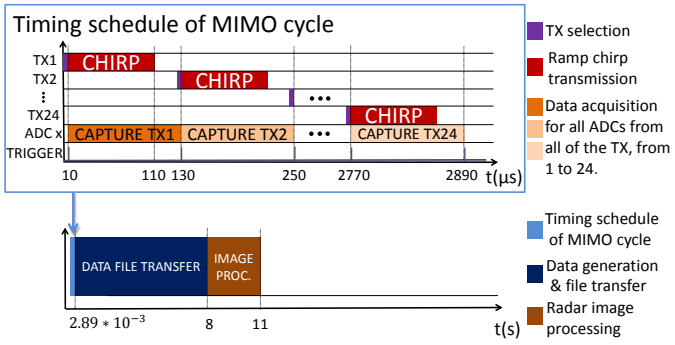

Fig. 19. Illustration of the timings for a complete MIMO cycle: transmission for all 24 TX elements, data acquisition, transfer and radar image processing.

in a round-robin fashion, with only one active at a time starting with TX1 and ending with TX24, is illustrated in Fig. 19. In this image, a complete FMCW MIMO cycle is represented from transmission to image generation. As it can be seen from the image, the frequency modulated chirp signals have a duration of $100\,\mu s$, a physical switching time of around $10\,ms$ and are sent sequentially with a delay of $20\,\mu s$. The received chirp signals at the RX array are then processed in parallel by means of multiplication with the transmitted chirp replica, before reaching the ADCs. The timing schedule for a complete MIMO cycle is, therefore, around 2.9 ms. Additionally, the time to process and transfer the 576 signals inside the digital unit and the radar image processing time itself need to be considered, which are around 8 s and 3 s, respectively for our current configuration. Consequently, as it can be understood, the main bottleneck of the system is the transferring of raw data through Ethernet to the processing system and the time for a single radar capturing and image reconstruction is in total around 11 s. Moreover, in order to speed up the radar image processing time, it is possible to specifically select the number of signals. For example, only 1 TX element and a row of 12 RX elements can be chosen, thus providing the ability to reconstruct the angles in only the azimuth axis, but decreasing the transferring and processing time.

As noted and expected, incoming reflections will have modulation from the previous modulation cycle. This imposes a range limit. Considering the timings until transmission of the next chirp, the formula for the two-way propagation delay from the radar to the target and back, sets a maximum range limit of [19]

$$r_u = t_{chirp}\frac{c_0}{2} = 18\,\mathrm{km} \tag{6}$$

where t_{chirp} represents the time duration from transmission of one chirp to the next. This value, called maximum unambiguous range, results from the remaining necessarily overlap of the transmission signal with the echo signal, to get enough time to measure a different frequency. Thus, there is always a sufficient time that allows the signals to be uncorrelated for the type of applications aimed with this system, ranging up to only several hundred meters.

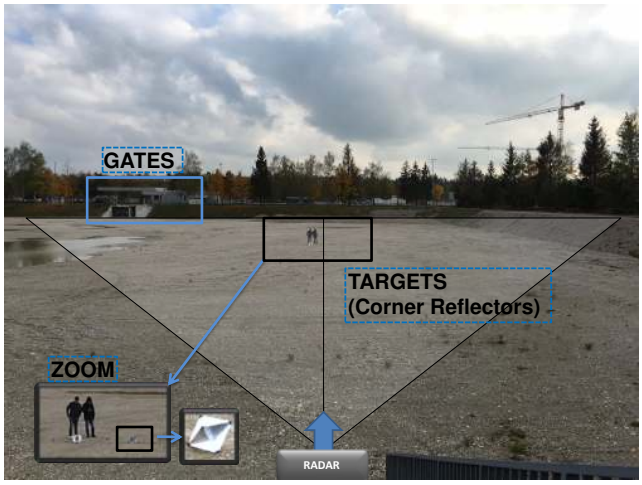

Fig. 20. The MIMO radar test field with two corner reflectors at a range of 60 m with nominal radar cross section (RCS) of $36\,m^2$.

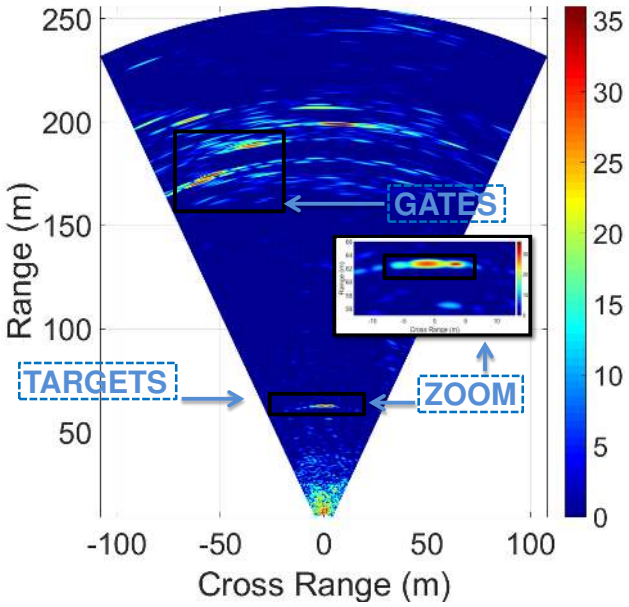

Fig. 21. Range-Azimuth section view of the 3D MIMO radar image capture from the radar setup scenario with two reflectors at a distance of 60 m.

V. System Performance and Results

To demonstrate the radar performance and its capabilities in generating a 3D image in multi-target scenarios, two radar test fields are set up with the use of corner reflectors. Only stationary radar scenarios have been investigated so far. The first test field, used for measuring the range and angular separation capabilities of the demonstrator, is shown in Fig. 20. In this test setup, in order to carry out the free space measurements with the FMCW MIMO radar demonstrator, two corner reflectors at a range of 60 m with nominal radar cross section (RCS) of $36\,m^2$ are placed in front of the radar at a slightly different orientation leading to differences in the measured RCS and different radial and lateral spacings.

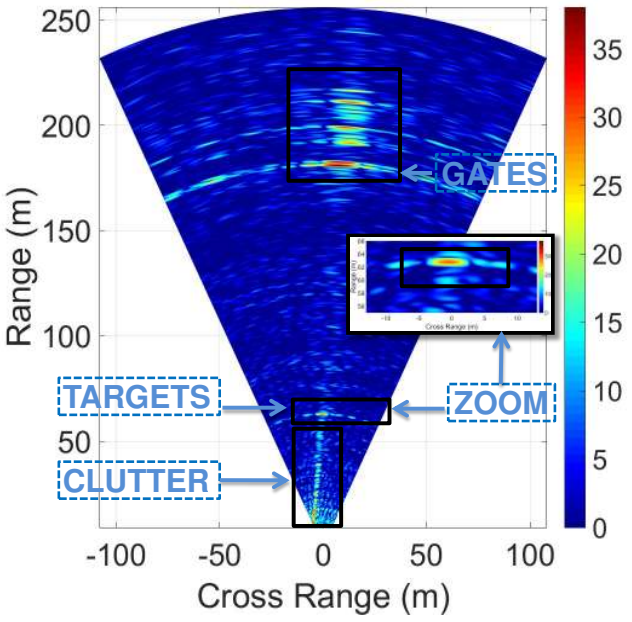

Fig. 22. Range-Elevation section view of the 3D MIMO radar image capture from the radar setup scenario with two reflectors at a distance of 60 m.

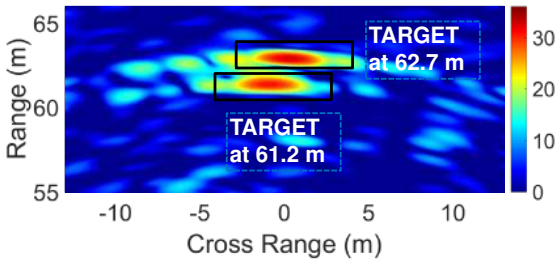

Fig. 23. Range-Azimuth section view of the 3D radar image capture, with DBF and MIMO processing, with the two corner reflectors placed at the same azimuth angle of around 0° and 1.5 m apart.

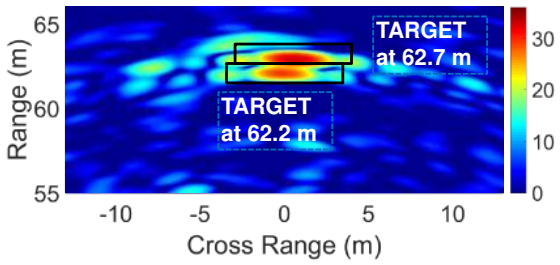

Fig. 24. Range-Azimuth section view of the 3D radar image capture, with DBF and MIMO processing, with the two corner reflectors placed at the same azimuth angle of around 0° and 0.5 m apart.

The people shown behind the reflectors serve the purpose of representing the size of the image compared to the scenario.

Each of the images is generated with 24 up-chirp signals ranging from 16 GHz to 17 GHz and with a duration of 100 µs. For easier understanding of the performance parameters, slices of the 3D images are presented in the following chapters, in the form of 2D images. The range-azimuth and range-elevation 2D section views are obtained by slicing the 3D image at $\phi = 0°$ and $\theta = 0°$, respectively.

A. Range, Azimuth and Elevation Estimation

A 2D radar image, cut in the azimuth plane, of the complete 3D image produced by the image reconstruction algorithm described in the previous section is shown in Fig. 21. In this example, the reflectors are placed within the same range cell at a distance of 60 m and at an angular distance of 4° (about 8 m lateral separation). It is possible to identify the two corner reflectors, together with additional reflections coming from two metal gates that were on the left at around 170 m distance from the radar, as shown in Fig. 20 and as it can also be seen from the FFT result presented in Fig. 18. The zoom into the targets in this image, makes it is easier to clearly identify and separate the 2 corner reflectors at 60 m range. The amplitude of the target on the right is 6 dB lower due to a non identical alignment of the used corner reflectors.

A 2D radar image, cut instead in the elevation plane, of the complete 3D image, is depicted in Fig. 22. In this image, the two corner reflectors can again clearly be seen. Considering that they are placed at the same elevation of 0° and at the same range, they can't be separated in this view. An important aspect to understand from this view are the clutter effects that can be seen as a line that starts from 0 m up to almost 60 m in range, which is ground clutter produced as reflected signals from the terrain. Since the radar is facing the two corner reflectors directly, but is positioned at an elevated position with respect to the terrain's level where the two corner reflectors are standing, clutter components starting from negative degree values of elevation are perfectly matching. The ground clutter eventually meets the elevation of the reflectors at around 60 m, as expected.

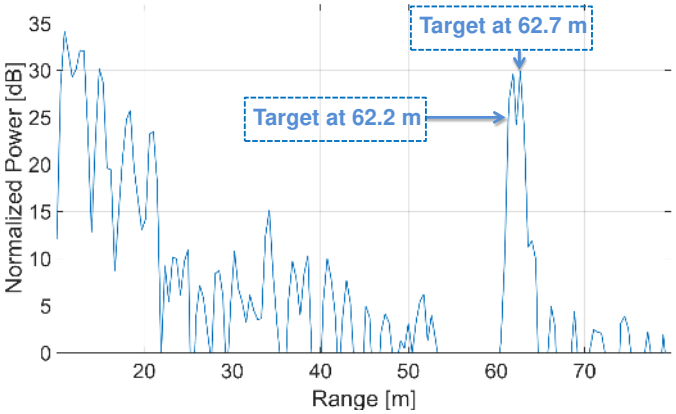

Fig. 25. FFT view of the 3D radar image capture, cut across ranges, with DBF and MIMO processing, with the two corner reflectors placed at the same azimuth angle of around 0° and 0.5 m apart.

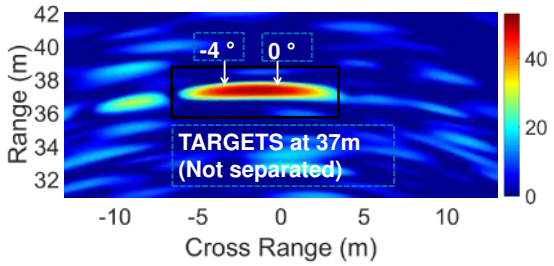

Fig. 26. Range-Azimuth section view of the 3D radar image capture, with conventional DBF and no MIMO processing. The corner reflectors are placed at an identical range cell. The two targets are not uniquely identifiable.

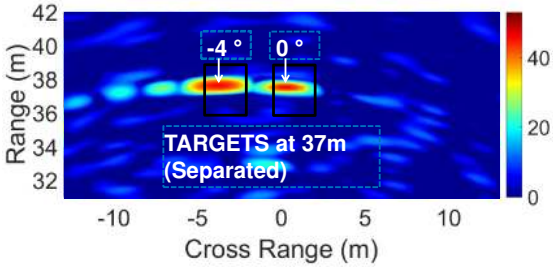

Fig. 28. Range-Azimuth section view of the 3D radar image capture, with DBF and MIMO processing. The corner reflectors are placed at an identical range cell. The two targets are uniquely identifiable.

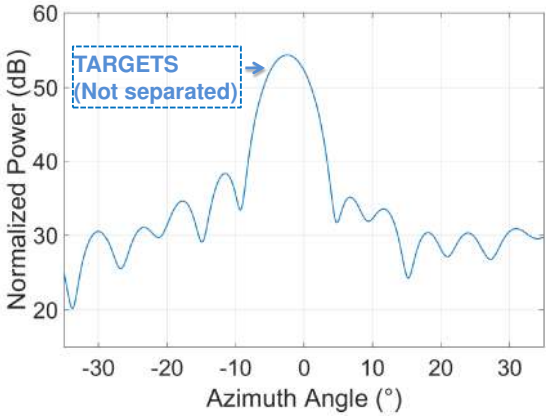

Fig. 27. dB - Angular section view of the 3D radar image capture, with conventional DBF and no MIMO processing. The corner reflectors are placed at an identical range cell. The two targets are not uniquely identifiable.

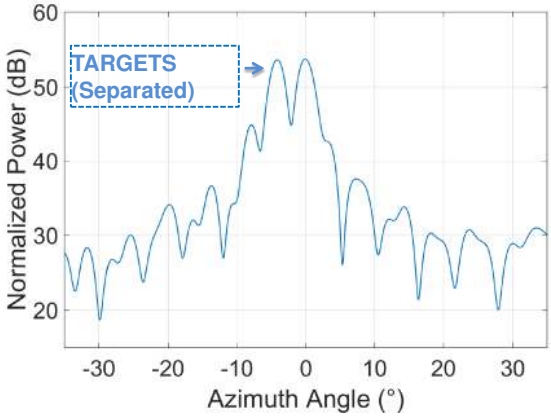

Fig. 29. dB - Angular section view of the 3D radar image capture, with DBF and MIMO processing. The corner reflectors are placed at an identical range cell. The two targets are uniquely identifiable.

B. Range Separation Capability

The achievable range resolution of a radar system depends mostly on the total bandwidth covered by the transmitted chirp signal. It is expressed as

$$\Delta r = \frac{c_0}{2B} \tag{7}$$

with c_0 being the speed of light and B the signal bandwidth. Considering a bandwidth of 1 GHz, equation (7) translates into $\Delta r = 15$ cm. However, because of non linearities in the generated chirp signals, truncation and range windowing, the effective range resolution is different. Considering that the measured bandwidth is $B_{eff} = 830$ MHz and that the Hanning window [20] entails a reduction of resolution by a factor of 1.5, the effective range resolution is $\Delta r = 27$ cm.

For the experimental determination of the range resolution, the corner reflectors are placed at an identical azimuth angle. Fig. 23 shows the results of a radar scenario with two targets at a radial distance of 1.5 m. Differently from the previously conducted measurement, by correctly orienting the corner cubes, their RCS has now been adjusted to be almost the same, even though some slight disparities are still to be expected due to fabrication processes of the corner cubes itself. Further reducing the radial distance to 0.5 m, gives instead the results shown in Fig. 24. Even though an expansion can be seen in the targets in the image caused by the applied Hanning window, the targets can still be considered uniquely identifiable. This is highlighted in Fig. 25, which depicts the FFT view of the 3D radar image, cut across the ranges and shows two distinctive peaks. This represents the closest tested distance that can be reached, in order to uniquely identify the targets. The linearity of the chirp signals is minimally affected by the frequency response of the RF front-end boards. This leads to a difference between the theoretical and measured range resolution of 1.48 %. Nevertheless, the achieved resolution is high enough for the intended application of the radar demonstrator, i.e. the surveillance of wide-zone scenarios.

C. Angular Separation Capability

The angular separation capability, previously described in Fig. 3 and equation (1), is now examined within a range cell, in the same scenario used in subchapter V-B, with two corner reflectors correctly oriented with same nominal radar cross section of $36\,\mathrm{m}^2$. However, now the targets are at a distance of 37 m. The system's ability to resolve multiple target scenarios is mainly determined by the width of the main lobe of the antenna, after DBF. As a result, the limiting factor for the angle separation capability is solely based on the width of

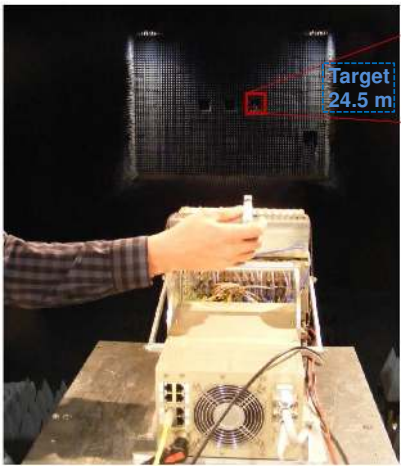

Fig. 30. Picture of the anechoic chamber for the measurement of the angular resolution. The target is placed at a distance of 24.5 m.

the shaped lobes and the angular resolution is approximately expressed as in equation (1). Although interpolation of the missing data is performed in order to address the missing data of the empty row of the virtual array illustrated in Fig. 3, which improves the overall resolution, differences between the measured angular resolution and the one given by equation (1) are expected to arise. This is due to the fact that the equation is an approximation based on a limited number of antenna elements and, additionally, weighting of antenna elements by means of classical windowing functions like the ones used in this algorithm, allows for better side lobe suppression, but at the expense of a slightly reduced angular resolution [20].

The processing of the collected data is carried out in two different ways. First, through conventional DBF by using only 1 transmit element and no virtual array with a Multiple-Input-Single-Output (MISO) approach and second, by using a MIMO processing approach. To determine the resolution limit, both reflectors are laterally moved toward each other, until the separation of the targets is no longer possible.

In Fig. 26 the conventional processing is used. As depicted in this figure, only a single target can clearly be seen in the middle of the detection area of the sensor. A corresponding range cut gives the graph shown in Fig. 27. Only one half-width main lobe is clearly visible, of 5.9°, which well matches the theoretical value determined by equation (1) of 5.79°. Therefore, since the beam-width is greater than the angular distance of the targets, a separation of the targets is not possible without MIMO processing.

Subsequently, the processing based on the MIMO virtual aperture is applied. The new calculated beam-width now translates into 2.89°. As previously mentioned, compared to the theoretical equation (1), this value is expected to be slightly different and in this case it is 0.39° higher. The results of the processing are shown in Fig. 28. It can now be seen, with a closer look as shown in Fig. 29, that the two close targets become more uniquely identifiable. Both targets are clearly visible at a distance of approximately 4°.

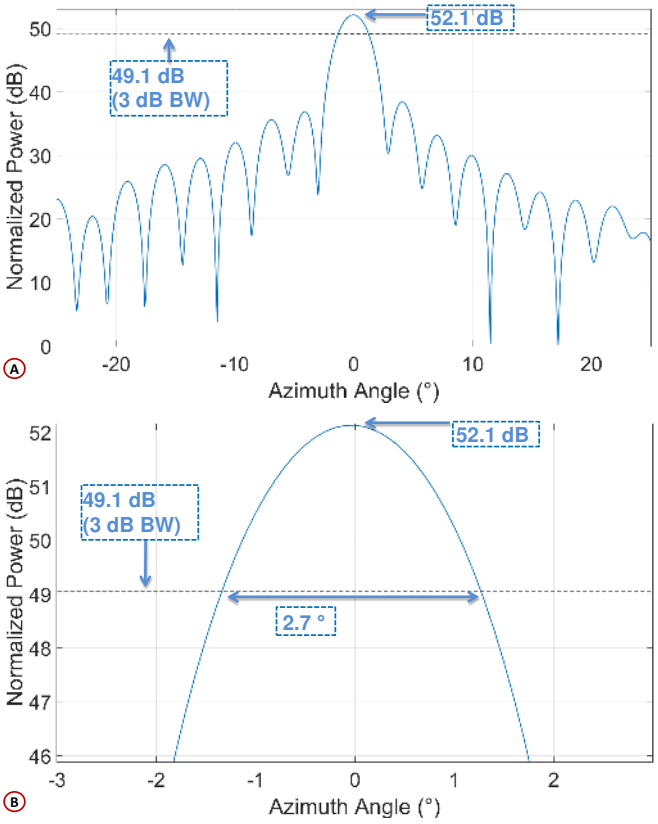

Fig. 31. dB - Angular section view of the 3D radar image capture of the target at 24.5 m, in the anechoic chamber.

Finally, in order to verify the results on the angular resolution from the field measurements, a further examination has been made inside an anechoic chamber, as it can be seen from Fig. 30. The target used in this case, is a corner reflector with a nominal radar cross section of $36\,\mathrm{m}^2$, that has been placed at an azimuth of $\theta = 0°$ and a range of 24.5 m. An angular section view, cut from the 3D radar image at $\phi = 0°$ and a range of 24.5 m, is shown in Fig. 31, subsection A. The angular resolution, calculated with MIMO processing, is taken as the 3 dB beam-width of the main lobe of the target. In this ideal scenario it becomes 2.7°, as shown in Fig. 31, subsection B. This value differs now only of 0.2° from the one given in equation (1), confirming an influence from the interpolation, the windowing and the fact that the equation is just an approximation.

D. Maximum Range

In order to measure the maximum range at which our radar demonstrator can identify a target, a corner reflector with nominal radar cross section of $36\,\mathrm{m}^2$ has been used and placed in an open field test scenario, at a distance of 315 m. As previously described and shown in Fig. 14, the transmit output power and the antenna gain of the radar are close to 20 dBm and 7 dB, respectively. A radar image, cut in the azimuth plane, of the complete 3D image is shown in Fig. 32. A zoom into the picture, shows that the target is clearly visible at a distance

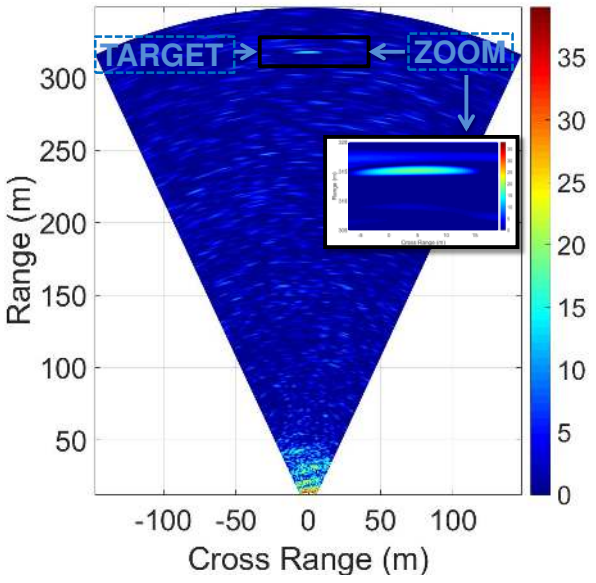

Fig. 32. Range-Azimuth section view of the 3D radar image capture, with 1 corner reflector visible at 315 m.

of 315 m, thus determining the maximum tested range of the radar system.

VI. State of the Art Comparison

A comparative research has been performed on the demonstrator structure and performance of other imaging radars already published. The results are presented in Table I.

To the best of our knowledge, there is currently only one device capable of generating a 3D image out of a 2D MIMO array configuration, described in [5]. Because of insufficient data presented in the papers analyzed regarding the target's RCS, it is difficult to extract a correct range information. Therefore, the devices are analyzed according to their ability to operate in short and medium range applications. From the first column of the table, it can be seen that it is intended for short range capturing, as observed from the high range and angular resolution but limited maximum range of the device of 1.5 m. Furthermore, limited by its large size, it is not portable.

The high performance of the 3D imaging proposed in this work, instead, can be seen in the last column of the table. This demonstrator is capable of operating in medium range radar scenarios, higher compared to the other 2D MIMO radar device analyzed in the table, nevertheless still maintaining a relatively high angular and range resolution of 2.9° and 0.5 m, respectively, thanks to its 1 GHz bandwidth. Moreover, a comparison study has been made considering the size of the devices. Considering medium sized portable devices, the radar demonstrator here proposed is the best in terms of resolutions. Additionally, the possibility of other devices of being modular and flexibly changeable in terms of MIMO array configuration has been investigated. The result is that there are currently no other 3D MIMO FMCW radar which have the capability of being modular.

TABLE I
Structure and performance comparison of different imaging radars.

	[5]	[12]	[13]	[14]	[15]	This Work
MIMO Array	YES	YES	YES	YES	YES	YES
2D MIMO Array	YES	NO	NO	NO	NO	YES
Freq. Ini. [GHz]	72	9.15	18	8.95	24	16
Freq. Fin. [GHz]	80	9.35	19	9.95	25	17
Bandwidth [GHz]	8	0.1	0.75	1	1	1
Max. Range	Short	Med.	Med.	Med.	Med.	Med.
Range Res. [m]	0.02	1.5	0.2	0.15	0.15	0.5
Angular Res. [°]	2.3	1.8	0.06	0.45	3	2.9
Modular	NO	NO	NO	NO	NO	YES
Size	Large	Med.	Large	Med.	Med.	Med.

VII. Conclusions

An innovative and successful implementation of a complete 3D imaging MIMO radar based on a 24x24 array architecture has been presented. The radar operates with a working frequency range between 16 GHz and 17 GHz and FMCW signals with 1GHz of bandwidth. The individual transmit signals are separated at the receiver using TDM and are digitally processed in hardware before applying the radar processing algorithms that generate the 3D radar images by means of digital beamforming techniques. A complete radar image can be generated in around 11 s, with the current configuration.

Furthermore, the demonstrator has been designed to be compact and portable by including its own power unit and cooling system. Since the radar system is intended to be flexible, a modular approach based on conventional low cost PCB is used for the transmit and receive boards. This modular approach is based on RF multilayer panels with integrated antennas, that are easily stackable in a sandwich configuration which grants the possibility to vary the number of antennas by removing or adding panels. This gives the ability to vary the angular resolution and the size of the radar.

In the proposed work, measurements of the components in both the TX and RX boards have been performed in order to ensure the proper operation of the system. Additionally, measurements of the coupling and its overall effect on system performance have been analyzed with satisfactory outcomes. Moreover, calibration, timing and performance analysis on the overall radar performance, especially regarding its separation capabilities for both, angle and range, have been carried out. Several resulting 2D profiles, proving the high resolution of the reconstructed images, have been presented. Based on the shown results, it can be seen that the full advantages brought by the use of a MIMO architecture have been achieved so far, which can be summarized as follows: reduced number of antenna elements and simpler RF distribution structure when compared to a conventional antenna array, compact design through high integration, in particular without complicated mechanics for beam steering and artificially enlarged aperture and thus, improved cross-resolution synthetic image generation.

VIII. Acknowledgment

The research leading to these results has partly received funding from the ZONeSEC Project, CP-IP-Large-Scale Integrating Project of the European Union's Seventh Framework Programme FP7-SEC-2013-1, under REA grant agreement n. 607292.

References

[1] M. Soumekh, "Synthetic aperture radar signal processing", New York, Wiley, 1999.

[2] E. Brookner, "Phased-array radars", Scientific American 252.2, pp. 94-102, 1985.

[3] J. Li and P. Stoica, "MIMO Radar Signal Processing", John Wiley & Sons, Inc., 2008.

[4] W. Wiesbeck, L. Sit, M. Younis, T. Rommel, G. Krieger and A. Moreira, "Radar 2020: The future of radar systems", 2015 IEEE International Geoscience and Remote Sensing Symposium (IGARSS), Milan, 2015, pp. 188-191.

[5] S. S. Ahmed, A. Schiessl and L. Schmidt, "Novel fully electronic active real-time millimeter-wave imaging system based on a planar multistatic sparse array", in *Microwave Symposium Digest (MTT), 2011 IEEE MTT-S International*, pp. 1-4, 5-10 June 2011.

[6] R. F. Rincon, M. A. Vega, M. Buenfil, A. Geist, L. Hilliard and P. Racette, "NASA's L-Band Digital Beamforming Synthetic Aperture Radar", in *IEEE Transactions on Geoscience and Remote Sensing*, vol. 49, no. 10, pp. 3622-3628, Oct. 2011.

[7] R. F. Rincon et al., "The EcoSAR P-band Synthetic Aperture Radar", in *2011 IEEE International Geoscience and Remote Sensing Symposium*, Vancouver, BC, 2011, pp. 1512-1515.

[8] G. Krieger, "MIMO-SAR: Opportunities and Pitfalls", in *IEEE Transactions on Geoscience and Remote Sensing*, vol. 52, no. 5, pp. 2628-2645, May 2014.

[9] M. T. Frankford, N. Majurec and J. T. Johnson, "Software-defined radar for MIMO and adaptive waveform applications", in *2010 IEEE Radar Conference*, Washington, DC, 2010, pp. 724-728.

[10] G. M. Brooker, "Understanding millimetre wave FMCW radars", in *1st international Conference on Sensing Technology*, Palmerston North, New Zealand, Nov. 21-23, 2005.

[11] A. Stove, "Linear FMCW Radar Techniques", in *Radar and Signal Processing, IEE Proceedings F*, vol. 139, no. 5, pp. 343-350, Oct. 1992.

[12] Y. Huang, P. V. Brennan, D. Patrick, I. Weller, P. Roberts, and K. Hughes, "FMCW based MIMO imaging radar for maritime navigation", in *Progress In Electromagnetics Research*, Vol. 115, 327-342, 2011.

[13] J. Klare, M. Weiss, O. Peters, A. R. Brenner and J. Ender, "ARTINO: A New High Resolution 3D Imaging Radar System on an Autonomous Airborne Platform", in *2006 IEEE International Symposium on Geoscience and Remote Sensing*, pp. 3842-3845, Denver, CO, USA, 2006.

[14] J. Klare, O. Saalmann, H. Wilden, and A. R. Brenner, "First Experimental Results with the Imaging MIMO Radar MIRA-CLE X", in *Synthetic Aperture Radar (EUSAR), 2010 8th European Conference on*, pp. 1-4, 7-10 Jun. 2010.

[15] W. Mayer, A. Gronau, W. Menzel and H. Leier, 'A Compact 24 GHz Sensor for Beam-Forming and Imaging,", in *2006 9th International Conference on Control, Automation, Robotics and Vision*, Singapore, pp. 1-6, 5-8 Dec. 2006.

[16] M. Harter, A. Ziroff and T. Zwick, 'Three-dimensional radar imaging by digital beamforming,", in *Radar Conference (EuRAD)*, Manchester, pp. 17-20, 12-14 Oct. 2011.

[17] X. Zhuge and A. G. Yarovoy, "A Sparse Aperture MIMO-SAR-Based UWB Imaging System for Concealed Weapon Detection", in *IEEE Transactions on Geoscience and Remote Sensing*, vol. 49, no. 1, pp. 509-518, Jan. 2011.

[18] R. Janaswamy, "Analysis of the tapered slot antenna", in *IEEE Transactions on Antennas and Propagation*, vol. 35, no. 9, pp. 1058-1065, Sep. 2003.

[19] M. Skolnik, "Radar Handbook, Third Edition", Electronics electrical engineering, McGraw-Hill Education, 2008.

[20] F.J. Harris, "On the use of windows for harmonic analysis with the Discrete Fourier Transform, in *Proceedings of the IEEE*, January 1978.

[21] T. Spreng, S. Yuan, V. Valenta, H. Schumacher, U. Siart and V. Ziegler, "Wideband 120 GHz to 140 GHz MIMO radar: System design and imaging results", in *Microwave Conference (EuMC), 2015 European*, Paris, pp. 430-433, 7-10 Sep. 2015.

[22] MACOM, "GaAs SPDT Switch DC - 20 GHz", MASW-008322, Rev-3, 2013.

[23] XILINX, "Virtex-5 Family Overview", DS100, Rev-5.1, 21 Aug. 2015.

[24] 4DSP, "FMC108 high pin count FMC ADC 8-channel 14-bit ADC - 250 MSPS", FMC108 Data-Sheet, Rev-1.1, June 2014.

[25] Freescale Semiconductor, "MPC8640 and MPC8640D Integrated Host Processor Hardware Specifications," MPC8640D, Rev-4, May 2014.

[26] A. Zwanetski, H. Rohling, "Continuous wave MIMO radar based on time division multiplexing", in *Radar Symposium (IRS), 2012 13th International*, pp. 119-121, 23-25 May 2012.

[27] T. Spreng, U. Prechtel, B. Schoenlinner, V. Ziegler, A. Meusling and U. Siart, "UWB near-field MIMO radar: Calibration, measurements and image reconstruction", in *Radar Conference (EuRAD), 2013 European*, Nuremberg, pp. 33-36, 9-11 Oct. 2013.